

# Roton pair density wave and unconventional strong-coupling superconductivity in a topological kagome metal

Hong-Jun Gao (✉ [hjgao@iphy.ac.cn](mailto:hjgao@iphy.ac.cn))

Institute of Physics <https://orcid.org/0000-0001-9323-1307>

Hui Chen

Institute of Physics, Chinese Academy of Sciences <https://orcid.org/0000-0002-3369-8113>

Haitao Yang

Institute of Physics

Bin Hu

Institute of Physics, Chinese academy of sciences

Zhen Zhao

Institute of Physics, Chinese academy of sciences

Jie Yuan

Institute of Physics, The Chinese Academy of Sciences, Beijing National Laboratory for Condensed Matter Physics

Yuqing Xing

Institute of Physics, Chinese academy of sciences <https://orcid.org/0000-0002-8646-6631>

Guojian Qian

Institute of Physics, Chinese academy of sciences

Zihao Huang

Institute of Physics, Chinese Academy of Sciences

Geng Li

Institute of Physics & University of Chinese Academy of Sciences, Chinese Academy of Sciences  
<https://orcid.org/0000-0002-3347-7222>

Yuhan Ye

Institute of Physics, Chinese Academy of Sciences

Sheng Ma

Institute of Physics, Chinese Academy of Sciences

Shunli Ni

Institute of Physics

Hua Zhang

Institute of Physics, Chinese Academy of Sciences

Qiangwei Yin

Renmin University of China

**Chunsheng Gong**

Renmin University of China

**Zhijun Tu**

Renmin University of China

**Hechang Lei**

Renmin University of China <https://orcid.org/0000-0003-0850-8514>

**Hengxin Tan**

Department of Condensed Matter Physics, Weizmann Institute of Science

**Sen Zhou**

Institute of Theoretical Physics, Chinese Academy of Sciences

**Chengmin Shen**

Institute of Physics

**Xiaoli Dong**

Beijing National Laboratory for Condensed Matter Physics and Institute of Physics, Chinese Academy of Sciences, Beijing 100190, China <https://orcid.org/0000-0002-6268-2049>

**Binghai Yan**

Weizmann Institute of Science <https://orcid.org/0000-0003-2164-5839>

**Ziqiang Wang**

Boston College

---

**Physical Sciences - Article**

**Keywords:** superconductivity, superconductors

**Posted Date:** March 25th, 2021

**DOI:** <https://doi.org/10.21203/rs.3.rs-355323/v1>

**License:**  This work is licensed under a Creative Commons Attribution 4.0 International License.

[Read Full License](#)

---

**Version of Record:** A version of this preprint was published at Nature on September 29th, 2021. See the published version at <https://doi.org/10.1038/s41586-021-03983-5>.

# **Roton pair density wave and unconventional strong-coupling superconductivity in a topological kagome metal**

Hui Chen<sup>1,2,3,4#</sup>, Haitao Yang<sup>1,2,3,4#</sup>, Bin Hu<sup>1,2#</sup>, Zhen Zhao<sup>1,2</sup>, Jie Yuan<sup>1,2</sup>, Yuqing Xing<sup>1,2</sup>, Guojian Qian<sup>1,2</sup>, Zihao Huang<sup>1,2</sup>, Geng Li<sup>1,2,3</sup>, Yuhan Ye<sup>1,2</sup>, Sheng Ma<sup>1,2</sup>, Shunli Ni<sup>1,2</sup>, Hua Zhang<sup>1,2</sup>, Qiangwei Yin<sup>5</sup>, Chunsheng Gong<sup>5</sup>, Zhijun Tu<sup>5</sup>, Hechang Lei<sup>5</sup>, Hengxin Tan<sup>6</sup>, Sen Zhou<sup>7,2,3</sup>, Chengmin Shen<sup>1,2</sup>, Xiaoli Dong<sup>1,2</sup>, Binghai Yan<sup>6</sup>, Ziqiang Wang<sup>8\*</sup>, and Hong-Jun Gao<sup>1,2,3,4\*</sup>

<sup>1</sup> Beijing National Center for Condensed Matter Physics and Institute of Physics, Chinese Academy of Sciences, Beijing 100190, PR China

<sup>2</sup> School of Physical Sciences, University of Chinese Academy of Sciences, Beijing 100190, PR China

<sup>3</sup> CAS Center for Excellence in Topological Quantum Computation, University of Chinese Academy of Sciences, Beijing 100190, PR China

<sup>4</sup> Songshan Lake Materials Laboratory, Dongguan, Guangdong 523808, PR China

<sup>5</sup> Beijing Key Laboratory of Optoelectronic Functional Materials & Micro-Nano Devices, Department of Physics, Renmin University of China, Beijing 100872, PR China

<sup>6</sup> Department of Condensed Matter Physics, Weizmann Institute of Science, Rehovot, Israel

<sup>7</sup> CAS Key Laboratory of Theoretical Physics, Institute of Theoretical Physics, Chinese Academy of Sciences, Beijing 100190, China

<sup>8</sup> Department of Physics, Boston College, Chestnut Hill, MA, USA

#These authors contributed equally to this work

\*Correspondence to: wangzi@bc.edu

hjgao@iphy.ac.cn

The recently discovered family of vanadium-based kagome metals with topological band structures offer new opportunities to study frustrated, correlated topological quantum states. These layered compounds are nonmagnetic and undergo charge density wave (CDW) transitions before developing superconductivity at low temperatures. Here we report the observation of unconventional superconductivity and pair density wave (PDW) in the vanadium-based kagome metal  $\text{CsV}_3\text{Sb}_5$  using scanning tunneling microscope/spectroscopy (STM/STS) and Josephson STS. The differential conductance exhibits a V-shaped pairing gap  $\Delta \sim 0.5$  meV below a transition temperature  $T_c \sim 2.3$  K. Superconducting phase coherence is observed by Josephson effect and Cooper-pair tunneling using a superconducting tip. We find that  $\text{CsV}_3\text{Sb}_5$  is a strong-coupling superconductor ( $2\Delta/k_B T_c \sim 5$ ) and coexists with long-range  $4a_0$  unidirectional and  $2 \times 2$  charge order. Remarkably, we discover a bidirectional PDW accompanied by  $4a_0/3$  spatial modulations of the coherence peak and gap-depth in the tunneling conductance. We term this novel quantum state a roton-PDW that can produce a commensurate vortex-antivortex lattice and account for the observed conductance modulations. Above  $T_c$ , we observe a large V-shaped pseudogap in the  $4a_0$  unidirectional and  $2a_0$  bidirectional CDW state. Electron-phonon calculations attribute the  $2 \times 2$  CDW to phonon softening induced structural reconstruction, but the phonon mediated pairing cannot describe the observed strong-coupling superconductor. Our findings show that electron correlations drive the  $4a_0$  unidirectional CDW, unconventional superconductivity, and roton-PDW with striking analogies and distinctions to the phenomenology of high- $T_c$  cuprate superconductors, and provide groundwork for understanding their microscopic origins in vanadium-based kagome superconductors.

The transition-metal kagome lattice materials are layered crystalline compounds where the transition-metal elements occupy the vertices of the two-dimensional networks of corner-sharing triangles. In contrast to the earlier interest in strongly correlated insulating kagome compounds such as the Herbertsmithite for quantum spin liquids and doped Mott insulators<sup>1-5</sup> where the geometrical frustration of antiferromagnetic order plays a dominant role, these transition-metal compounds are correlated metals with itinerant electrons hosted by the kagome lattice electronic structures. Due to the special geometry impacting the quantum interference, the latter possess Dirac points and nearly flat bands that naturally promote topological and correlation effects, providing exciting opportunities for exploring frustrated, correlated, and topological quantum states of matter. Remarkable correlated topological phenomena, including massive spin-polarized Dirac fermions<sup>6-8</sup>, magnetic Weyl semimetal<sup>9-11</sup>, topological Chern magnet<sup>12</sup>, negative flat band orbital magnetism<sup>13</sup> and spin-orbital polarons<sup>14</sup>, have been observed in the class of Fe-, Co-, and Mn-based magnetic transition-metal kagome shandites.

Recently, a new family of vanadium-based kagome metals  $AV_3Sb_5$  ( $A=K, Rb, \text{ and } Cs$ ) has been discovered<sup>15</sup>, which were predicted to have  $Z_2$  nontrivial topological band structures with topological surface states by density functional theory<sup>15,16</sup>. They are nonmagnetic metals<sup>17</sup> that undergo charge density wave (CDW) transitions below  $T_{cdw} \sim 78 - 103$  K and superconducting (SC) transitions below  $T_c \sim 0.9 - 2.5$  K<sup>16,18,19</sup>. The CDW states are intriguingly structured<sup>20-22</sup> and exhibit unconventional anomalous Hall effect<sup>23,24</sup> usually found only in ferromagnetic materials. There is evidence for unconventional charge order that breaks the time-reversal symmetry<sup>20</sup> and proximity-induced spin-triplet pairing, pointing to an unconventional superconductivity<sup>25</sup>. Aside from the transport evidence for gap nodes<sup>26</sup> and gapless core states in magnetic-field induced vortices<sup>22</sup>, the nature of the SC ground state and its relation to the CDW states have not been explored.

Here, we study the ground state and low-temperature properties of  $CsV_3Sb_5$  with the highest bulk  $T_c$  ( $\sim 2.5$  K) using an ultra-low-temperature scanning tunneling microscope/spectroscopy (STM/STS) and Josephson STS. On cleaved surfaces, SC phase coherence is observed by the Josephson effect. We find strong-coupling unconventional superconductivity with a V-shaped SC gap that coexists with long-range  $4a_0$  unidirectional and  $2 \times 2$  charge order, i.e. a smectic superconductor that breaks both translation and rotational symmetry of the kagome lattice. More strikingly, we discover an emergent pair density wave

(PDW), dubbed a roton-PDW, that governs a novel  $4a_0/3$  bidirectional spatial modulation of the differential conductance with anti-correlated SC coherence peak height and density of gapless excitations. The long-range ordered  $4a_0$  unidirectional charge order and  $2\times 2$  CDW persists above  $T_c$  where we observe a large V-shaped pseudogap in the density of states. The striking analogies and distinctions to the phenomenology of the cuprate high- $T_c$  superconductors are provocative and revealing<sup>27-31</sup>.

## Results

$\text{CsV}_3\text{Sb}_5$  has a stacking structure of Cs-Sb2-VSb1-Sb2-Cs layers with hexagonal symmetry (space group P 6/mmm) (Fig. 1a). In the VSb1 layer, the kagome net of vanadium is interwoven with a simple hexagonal net formed by the Sb1 sites (Fig. 1b). The Cs and Sb2 layers form hexagon and honeycomb lattices, respectively (Fig. 1b). Scanning electron microscope combined with energy-dispersive x-ray spectroscopy and x-ray powder diffraction spectra demonstrate that the as-grown  $\text{CsV}_3\text{Sb}_5$  crystals are of high quality (Fig. S1). To characterize the bulk electronic properties, we measure the temperature dependent magnetization, resistivity, and heat capacity of the sample, as shown in the Supplemental Information (Fig. S2). All measurements indicate the presence of an anomaly at  $T_{\text{cdw}} \sim 94$  K (Fig. S2) associated with the CDW transition<sup>16,24</sup>. At low temperatures, the magnetization, resistivity, and heat capacity measurements show a transition to the SC state at a critical temperature of  $T_c \sim 2.8$  K. The somewhat higher  $T_c$  than the one reported in the literature (2.5 K)<sup>16</sup> is consistent with the high quality of the as-grown  $\text{CsV}_3\text{Sb}_5$  sample, which provides the opportunity for deeper understanding of the nature of superconductivity and coexisting electronic order through atomically-resolved STM/S.

Weak bonds between Cs and Sb2 layers offer a cleave plane and make it possible to have Cs-terminated and Sb-terminated surfaces. In the STM measurements at 4.2 K, we predominantly observe both types of the surfaces. At the interface of the two surfaces, we clearly identify the atomic structures on both the top and bottom surfaces using high-resolution STM (Figs. 1c, 1d). We find that the lattice in the bottom layer shows a honeycomb configuration, which is in agreement with that of Sb2 layer, while the top surface shows a hexagonal lattice with a space of 1 nm, which is about  $\sqrt{3}$  larger than the lattice constant. Based on the crystal structure shown in Fig. 1a, we attribute the bottom and top sublayers to the Sb2 and Cs surfaces, respectively. From the lattice constant and orientation in the STM image and the corresponding

Fast Fourier transform (FFT) patterns, we identify the two cleaved terminations as  $\sqrt{3}\times\sqrt{3}R30^\circ$  reconstructed Cs surface and  $1\times 1$  Sb surface (Fig. 1d, details in Fig. S3).

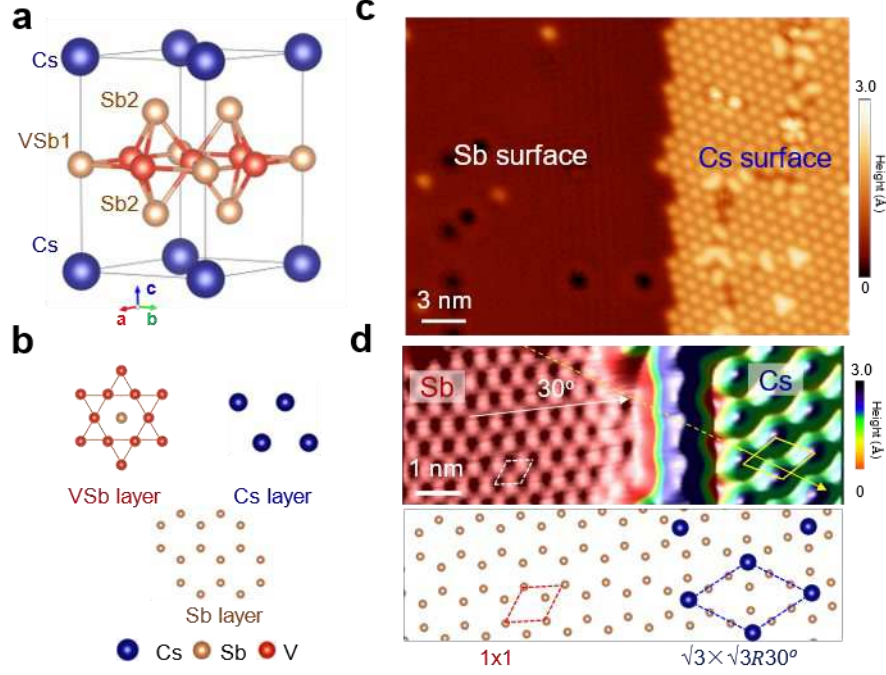


**Fig. 1. Atomic structures and the surface identification of the CsV<sub>3</sub>Sb<sub>5</sub>.** **a**, 3D view of crystal structure, showing stacking of Cs-Sb<sub>2</sub>-VSb<sub>1</sub>-Sb<sub>2</sub>-Cs layers with hexagonal symmetry. **b**, Atomic structures of VSb, Cs and Sb layers. **c**, Typical large-scale STM image, showing the Cs surface and Sb surface, respectively (scanning setting: bias:  $V_s = -1.0$  V, setpoint  $I_t = 100$  pA). **d**, Typical atomically-resolved STM image, showing the atomic structures of the Cs surface and the Sb surface, respectively ( $V_s = -0.5$  V,  $I_t = 500$  pA). Bottom panel: schematic of the atomic structures of the Sb and Cs surfaces, showing  $1\times 1$  and  $\sqrt{3}\times\sqrt{3}R30^\circ$  reconstructed structures, respectively.

We first study the SC ground state using STS at the electron temperature  $T_{\text{electron}} = 300$  mK. The electron temperatures are calibrated on the (110) surface of a well-known s-wave superconductor Nb (Fig. S4) prior to the measurements. We observe particle-hole symmetric V-shaped gaps in the differential conductance near the Fermi level ( $E_F$ ). The spatially-averaged  $dI/dV$  spectra (Fig. 2a) show the V-shaped gap on both Cs and Sb surfaces with two gap-edge peaks at energies symmetric with respect to  $E_F$ . The V-shaped gap is consistent with the gap nodes seen in the thermal transport<sup>26</sup>, but the non-zero local density of states (LDOS) at zero-bias, lower on the Sb than the Cs surface (Fig. S5), indicates possible

line nodes, ungapped Fermi surface sections, or additional in-gap states. From the  $dI/dV$  spectra collected over nearly fifty  $30\text{ nm}\times 30\text{ nm}$  regions, we obtain the average gap size  $\Delta \sim 0.52\pm 0.1\text{ meV}$  (Fig. S6). The temperature evolution of the  $dI/dV$  spectra on the Cs surface (Fig. 2b) show that the V-shaped gap reduces with increasing electron temperature and vanishes around  $\sim 2.3\text{ K}$ .

Since the suppression of the LDOS near  $E_F$  can result from physics other than superconductivity<sup>32,33</sup>, it is crucial to directly probe the superfluid for superconducting phase coherence by using a SC STM tip. If the sample surface is SC, a superconductor-insulator-superconductor (SIS) junction naturally forms under the tip for SIS tunneling. This is known as a Josephson STM. In this case, the SC tip and sample are coupled by the Josephson coupling  $E_J$  as the tip approaches sufficiently close to the sample at temperatures below the transition temperature of both the tip and sample. At temperatures  $k_B T > E_J$ , the thermally fluctuating Cooper pairs tunnel and give rise to a tunneling current directly proportional to the phase difference of the SC order parameters between the tip and the sample. Therefore, the Josephson effect, with a sharp zero-bias peak accompanied by two side negative differential dips, is a hallmark for the existence of superconductivity<sup>34-36</sup>.

We thus construct a Josephson STM (Fig. 2c) by fabricating a SC Nb STM tip (see the SC tip calibration in Fig. S7). When the Nb tip approaches sufficiently close to the surface, a sharp zero-bias peak with two negative differential conductance dips are observed (Fig. 2d), which provides strong evidence that the  $\text{CsV}_3\text{Sb}_5$  surface is in the SC phase (more data in Fig. S8). Based on the observed  $dI/dV$  spectra associated

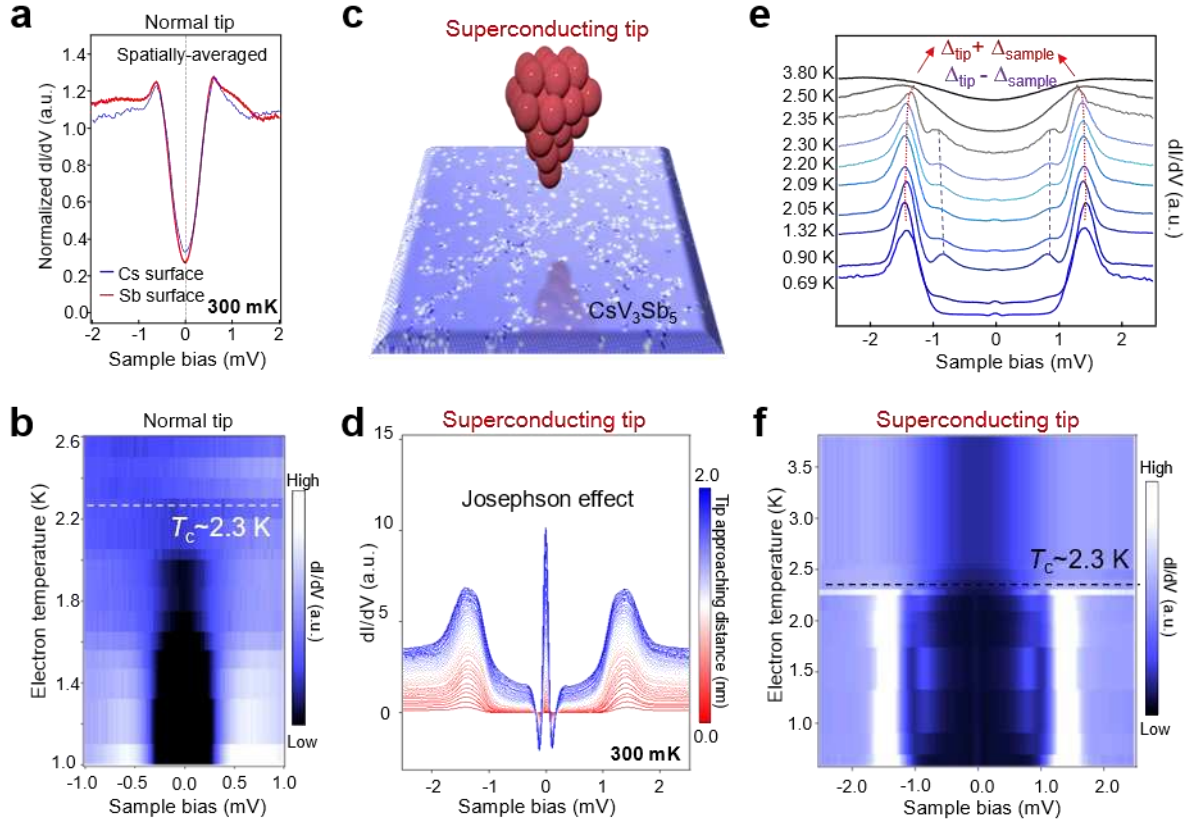


**Fig. 2. V-shaped pairing gap and the Josephson effect observed using a superconducting STM tip on the Cs and Sb surfaces.** **a**, Spatially-averaged  $dI/dV$  spectra obtained on the Cs and Sb surfaces over a  $30 \text{ nm} \times 30 \text{ nm}$  region with small defect density at the  $T_{\text{electron}} = 300 \text{ mK}$ , showing a particle-hole symmetric V-shaped gap near  $E_F$  and non-zero LDOS at zero-bias ( $V_s = -2 \text{ mV}$ ,  $I_t = 1 \text{ nA}$ ,  $V_{\text{mod}} = 50 \text{ } \mu\text{V}$ ). **b**, Color map of temperature dependent  $dI/dV$  spectra obtained on the Cs surface, showing that the V-shaped gap reduces with increasing electron temperature and vanishes around  $\sim 2.3 \text{ K}$  (dotted white line) ( $V_s = -2 \text{ mV}$ ,  $I_t = 1 \text{ nA}$ ,  $V_{\text{mod}} = 50 \text{ } \mu\text{V}$ ). **c**, Schematics showing the Josephson STM on  $\text{CsV}_3\text{Sb}_5$  surface using a superconducting (Nb) tip. **d**, A series of  $dI/dV$  spectra with approaching tip toward sample surface. A sharp zero-bias peak with two negative differential conductance dips are observed, providing strong evidence that the  $\text{CsV}_3\text{Sb}_5$  is in the SC phase ( $V_s = -2.5 \text{ mV}$ ,  $V_{\text{mod}} = 50 \text{ } \mu\text{V}$ ). **e**, Temperature dependent  $dI/dV$  spectra on the Cs surface using a Nb tip, showing two energy gaps at  $\Delta_{\text{tip}} + \Delta_{\text{sample}}$  and  $\Delta_{\text{tip}} - \Delta_{\text{sample}}$ , respectively ( $V_s = -2.5 \text{ mV}$ ,  $I_t = 20 \text{ nA}$ ,  $V_{\text{mod}} = 50 \text{ } \mu\text{V}$ ). **f**, Color map of the  $dI/dV$  spectra in (e), showing the transition temperature of the  $\text{CsV}_3\text{Sb}_5$  sample around  $\sim 2.3 \text{ K}$  ( $V_s = -2.5 \text{ mV}$ ,  $I_t = 20 \text{ nA}$ ,  $V_{\text{mod}} = 50 \text{ } \mu\text{V}$ ).

with the Josephson effect, we estimate the Josephson energy  $E_J = 1.61 \text{ } \mu\text{eV}$  and the charging energy  $E_C = 160 \text{ } \mu\text{eV}$ , which allows the thermal energy to satisfy  $E_J < E_T < E_C$  ( $E_T = k_B T = 25.8 \text{ } \mu\text{eV}$  at the electron temperature  $300 \text{ mK}$ ). Thus, the zero-bias peak can be well explained by Cooper pair tunneling in the fluctuation dominated Josephson regime<sup>34-40</sup>. The Josephson STM is then used to obtain

the temperature dependent  $dI/dV$  spectra at a relatively small tip-sample distance where the Josephson effect induced zero-bias peak is still present (Figs. 2e, 2f). When the electron temperature increases to about 900 mK, two sets of peaks can be clearly resolved with particle-hole symmetry. The outer peaks correspond to the sum  $\Delta_{\text{tip}} + \Delta_{\text{sample}}$  of the pairing gaps in the tip and the sample, while the inner peaks relate to the difference  $\Delta_{\text{tip}} - \Delta_{\text{sample}}$ . Upon further increasing the temperature, the inner peaks disappear at a transition temperature of  $\sim 2.3$  K, leaving the two remaining peaks from  $\Delta_{\text{tip}}$ . Since the  $T_c$  of the tip should be higher than 4 K (Fig. S7), such a transition indicates that superconductivity in the sample is totally suppressed at this temperature. The SC gap and critical temperature of the sample are in excellent agreement with the value from the V-shaped gap measured by the normal W tip. Therefore, we conclude that the observed V-shaped gap (Fig. 2a) is the SC gap that opens at a  $T_c \sim 2.3$  K on the surface of the  $\text{CsV}_3\text{Sb}_5$ . The V-shaped SC gap with non-zero LDOS at  $E_F$  is strongly indicative of unconventional superconductivity<sup>41,42</sup>. Moreover, the measured gap-to- $T_c$  ratio  $2\Delta/k_B T_c \sim 5.2$  puts the unconventional superconductor in the strong-coupling regime.

To investigate the unique nature of the unconventional SC state, we next probe the spatial distribution of the off-diagonal long-range ordered quantum states using the high-resolution STM/STS at an electron temperature 300 mK well below  $T_c$ . Since the Cs atoms are unstable on the Cs terminated surface and strongly affect the tip states, we perform the measurements on the Sb surface directly above the V kagome plane. The low temperature STM topography (Fig. 3a) shows intricate periodic lattice modulations with a clear unidirectional character. The FFT (Fig. 3b) reveals that in addition to the atomic Bragg peaks  $\mathbf{Q}_{\text{Bragg}}^{(a,b)}$  of the pristine Sb lattice, two sets of new peaks are present. One set comprises the six hexagonal wave vectors at  $\mathbf{Q}_{3q-2a} = (1/2)\mathbf{Q}_{\text{Bragg}}$ , corresponding to a  $2 \times 2$  superstructure on the kagome lattice. The other set is at axial wave vectors marked by  $\mathbf{Q}_{1q-4a}$ , corresponding to unidirectional  $4a_0$  modulations. These suggest the coexistence of superconductivity with  $2a_0$  bidirectional and  $4a_0$  unidirectional electronic positional and rotational order, i.e. a smectic state in the language of liquid crystals<sup>43,44</sup>. The  $dI/dV$  maps obtained over the same region are displayed at three energies around the SC gap (Figs. 3c, 3e, 3g). The charge stripes running along one of the two lattice directions with  $4a_0$  spacing are self-evident in all three LDOS maps. There are also less prominent features clearly revealed in the corresponding FFT patterns (Figs. 3d, 3f, 3h). The two sets of ordering wave vectors seen in the topography (Fig. 3b) are both sharply peaked at  $\mathbf{Q}_{3q-2a}$  and  $\mathbf{Q}_{1q-4a}$  in the  $dI/dV$  maps. Moreover, the positions of these vectors do not disperse in

energy (Fig. S9), leading us to conclude that they correspond to the  $2 \times 2$  and  $4a_0$  unidirectional CDW orders coexisting with the smectic superconductor.

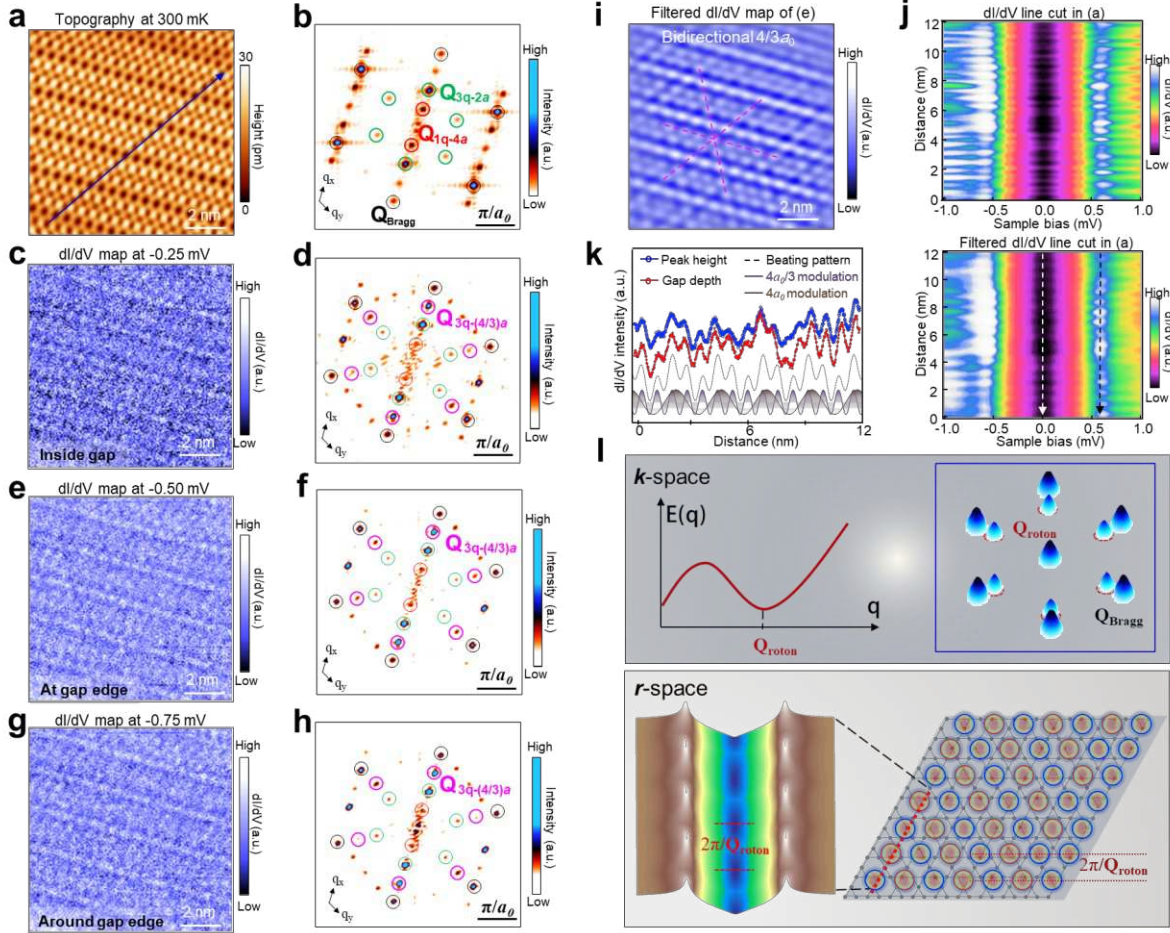


**Fig. 3. Spatial distribution of quantum electronic states on Sb surface at  $T_{\text{electron}}=300$  mK.** **a**, Typical atomically-resolved STM topography of Sb surface ( $V_s=-90$  mV,  $I_t=2$  nA). **b**, FFT of (a), showing clearly wave vectors  $\mathbf{Q}_{3q-2a}$  associated with  $2 \times 2$  CDW and  $\mathbf{Q}_{1q-4a}$  associated with  $4a_0$  unidirectional charge order. **c**, **e**, **g** dI/dV maps of (a) at  $-0.25$  meV,  $-0.5$  meV and  $-0.75$  meV, respectively ( $V_s=-90$  mV,  $I_t=2$  nA,  $V_{\text{mod}}=0.2$  mV). **d**, **f**, **h** FFT patterns corresponding to (c), (e) and (g), respectively. Besides the  $\mathbf{Q}_{3q-2a}$  and  $\mathbf{Q}_{1q-4a}$  charge ordered states present in the topography (a, b), a new  $4a_0/3$  bidirectional modulation emerges at  $\mathbf{Q}_{3q-4/3a}$ . **i**, The dI/dV map near the pairing gap in (e) after filtering out atomic Bragg peaks at  $\mathbf{Q}_{\text{Bragg}}$  and incoherent background, showing  $4a_0/3$  checkerboard modulations associated with the bidirectional PDW. **j**, Image plot of the dI/dV curves along a line cut in the lattice direction shown in (a), before (upper panel) and after (lower panel) filtering ( $V_s=-1$  mV,  $I_t=4$  nA,  $V_{\text{mod}}=20$   $\mu$ V). **k**, Spatial modulations of the coherence peak height (blue curve) along the black arrow in (j) and the SC gap-depth (red curve) obtained by subtracting the zero-bias conductance along the white arrow in (j) from the peak height, showing strong positive correlation between the two curves. The simulated curve based on  $\mathbf{Q}_{1q-4a}$  (brown curve) and  $\mathbf{Q}_{3q-4/3a}$  (purple curve) modulations shows a beating pattern consistent with the coherence peak height and gap-depth modulations. **l**, Schematic illustrations of the roton-PDW. Top panel: the roton dispersion and

minimum at  $\mathbf{Q}_{\text{roton}}$  in the reciprocal lattice. Bottom panel: the bidirectional roton-PDW at  $\mathbf{Q}_{\text{pdw}} = \mathbf{Q}_{\text{roton}}/2$  forming a commensurate vortex-antivortex (blue and red circles) lattice that spatially modulates the tunneling conductance spectra along a line cut.

A striking feature of the  $dI/dV$  maps, *absence* in the topography, is the new set of prominent peaks at hexagonal wave vectors  $\mathbf{Q}_{3q-4a/3} = 3\mathbf{Q}_{\text{Bragg}}/4$  in the FFT patterns (Figs. 3d, 3f, 3h). These peaks do not exist in the topography (Fig. 3b), nor in the  $dI/dV$  maps at energies much higher than the SC gap energy (Fig. S10). They strongly suggest an emergent  $4a_0/3$  bidirectional electronic modulations in the SC state without long-range charge order at  $\mathbf{Q}_{3q-4a/3}$ . The  $\mathbf{Q}_{3q-4a/3}$  peaks in the FFT of the  $dI/dV$  map are nondispersive at low energies around the SC gap, indicating the possible formation of a primary bidirectional PDW order. This is in contrast to the long-range CDW orders at  $\mathbf{Q}_{3q-2a}$  and  $\mathbf{Q}_{1q-4a}$  that induce subsidiary pair PDWs at the same wave vector in the background SC state by symmetry<sup>27,28,31,45-47</sup>. To reveal the spatial pattern of the PDW, the  $dI/dV$  map at -0.5 mV (Fig. 3e) is reproduced in Fig. 3i after Fourier filtering out the atomic Bragg peaks at  $\mathbf{Q}_{\text{Bragg}}$  and the noise from quasiparticle scattering (Fig. S12). A hexagonal checkerboard pattern of the bidirectional PDW is clearly observed, superimposed in the background of unidirectional  $4a_0$  charge stripes.

To investigate the properties of the PDW, the  $dI/dV$  spectra are measured along a line cut indicated in Fig. 3a, the  $q_x$ -direction in the reciprocal space (Fig. 3b), and shown as a differential conductance map in Fig. 3j. After filtering out the atomic Bragg oscillations and background noise, the coherence peaks at the gap energy ( $\sim \pm 0.5$  mV) and the zero-bias conductance at the bottom of the gap show intriguing spatial variations. The spatial modulation of the coherence peak height and the SC gap-depth obtained by subtracting the zero-bias conductance from the peak height (Fig. 3k) exhibit the remarkable beating pattern of two primary frequencies corresponding to the  $4a_0$  wavelength driven by the unidirectional CDW and the  $4a_0/3$  wavelength associated with the bidirectional PDW. The strong positive correlation between the two curves indicates that a higher coherence peak, which in STS usually reflects a higher superfluid density<sup>28</sup>, is concomitant with a deeper SC gap and less normal fluid density (See Fig. S11 for more analysis). This supports the scenario that the emergent PDW is a novel intertwined density wave order of both the superfluid and the normal fluid, such that the total electron density is approximately unmodulated

at the bidirectional wave vector  $\mathbf{Q}_{3q-4a/3}$ . This is likely the reason behind the rather uniform SC gap, showing little or no systematic variation along the line cut (Fig. 3j, bottom panel).

The observation of the emergent density wave order in the SC ground state is consistent with the existence of a shallow roton minimum at  $\mathbf{Q}_{\text{roton}} = \mathbf{Q}_{3q-4a/3}$  in the dynamical density-density response function of the superfluid (Fig. 3l, top panel). The roton gap protects the superfluid from crystallization, allowing only short-ranged itinerant charge density correlations at this wave vector. The incipient bidirectional PDW order is described by an inhomogeneous order parameter  $\Delta_{\mathbf{Q}_{\text{pdw}}}(\mathbf{r})$  with a wave vector  $\mathbf{Q}_{\text{pdw}} = \frac{1}{2} \mathbf{Q}_{\text{roton}}$ . Thus, the intertwined density wave order has the character of delocalized Cooper pair excitations and localized charge excitations. To stress this distinction, we refer to this new quantum state imprinted with the roton character as a roton-PDW. This scenario suggests that CsV<sub>3</sub>Sb<sub>5</sub> is close to incipient crystallization with low energy excitations involving both nodal quasiparticles and the roton-PDW excitations. Since a roton is a bound vortex-antivortex pair<sup>48-51</sup>, the bidirectional roton-PDW can be viewed as a commensurate hexagonal vortex-antivortex lattice (Fig. 3l, lower panel) pinned by the zeroes in the PDW order parameter  $\Delta_{\mathbf{Q}_{\text{pdw}}}(\mathbf{r})$  and coexists with the uniform component of the SC order parameter. Such an unconventional SC state would necessarily have a complex pairing order parameter that breaks time-reversal symmetry, exhibiting spontaneous phase windings associated with  $\Delta_{\mathbf{Q}_{\text{pdw}}}(\mathbf{r})$  and unconventional SC vortices<sup>31,45</sup>. The roton-PDW provides a qualitative explanation for our observations. The low energy states inside the V-shaped SC gap in the LDOS (Fig. 2a) are primarily localized vortex-antivortex core states, while the itinerant nodal quasiparticles contribute to the thermal transport<sup>26</sup>. The spatial modulation of the coherence peak height and gap-depth can be accounted for by those in the local superfluid density and the anti-correlated normal fluid density on the vortex-antivortex lattice (Fig. 3l, lower panel), without requiring modulations of the SC gap-size.

Finally, we warm up the sample to 4.2 K and explore the normal state following the melting of superconductivity. The atomically-resolved STM topography (Fig. 4a) and corresponding FFT patterns (Fig. 4b) are similar to that in the SC ground state (Fig. 3a, 3b), indicating the persistence of the  $4a_0$  unidirectional charge order into the normal state. To probe the electronic states, we measure  $dI/dV$  maps at different energies. A typical  $dI/dV$  map is shown at 50 mV with single-atom resolution in Fig. 4c and

the FFT in Fig. 4d. In addition to the atomic Bragg peaks, the  $2a_0$  bidirectional and  $4a_0$  unidirectional patterns are clearly observed. However, the Fourier peaks associated with the  $4a_0/3$  bidirectional PDW order have disappeared. This confirms the absence of long-range PDW order above  $T_c$ . The  $2\times 2$  and  $4a_0$  stripe patterns are observed in the  $dI/dV$  maps in the energy range from 0 mV to 90 mV and the ordering wave vectors in the corresponding FFT at  $\mathbf{Q}_{3q-2a}$  and  $\mathbf{Q}_{1q-4a}$  are nondispersive in energy (Fig. 4e). We thus conclude that the  $2\times 2$  CDW, and in particular the  $4a_0$  unidirectional charge order persist above  $T_c$ , which has been observed independently in the recent STM work<sup>21</sup>. We carry out DFT calculations and find that the three-dimensional  $2\times 2\times 2$  CDW arises from phonon softening and electron-phonon coupling in all  $AV_3Sb_5$ <sup>52</sup>. The phonon spectrum showing mode softening in  $CsV_3Sb_5$  is reproduced in Fig. S13. Combining the theory and experiments, we believe the  $2\times 2$  CDW order is robust and extends from the SC ground state all the way up to  $T_{cdw}$ <sup>21</sup>. However, we find that the electron-phonon coupling mediated superconductivity obtained by solving the McMillan equation in the reconstructed lattice structure cannot describe the observed strong-coupling superconductor<sup>52</sup>.

The  $4a_0$  unidirectional charge order, on the other hand, does not emerge in the electron-phonon coupling picture alone and is most likely also driven by electron correlations. The axial  $4a_0$  order breaks the lattice rotation symmetry. We perform angular-dependent resistance measurements and clearly observe the twofold symmetry with the anisotropy axis along one of the lattice directions (Fig. S14). We find that the pinning of the  $4a_0$  unidirectional charge order is weak as it can be spatially manipulated by the tip-induced electric field. As the STM tip scans along one lattice direction, the positions of the stripes can be spatially shifted along the same direction. Occasionally, the distance between two neighboring stripes changes from  $4a_0$  to  $5a_0$  (Fig. S15). The survival of charge order above  $T_c$  raises the question whether a pseudogap exists in the normal state. To gain further insights into the electronic structure, the spatially-averaged  $dI/dV$  spectrum is shown in Fig. 4f and compared to the DFT band structure in the pristine state (Fig. 4g). There is a broad suppression of the LDOS at  $\sim -0.20$  V, which matches the Dirac points (DPs) in the calculated dispersions. Moreover, there are two peaks/breaks in the LDOS within 100 mV below the Fermi level that match well with the two van Hove singularity (VHS) points marked in the band dispersions. Zooming in to low energies (Fig. 4f, inset) reveals a sharp, approximately V-shaped pseudogap density of states suppression between -10 mV and 10 mV. We thus attribute this normal state pseudogap to the CDW ordering. The existence of the  $4a_0$  unidirectional charge order at low temperatures and its melting above

a characteristic temperature  $T^* \sim 60 \text{ K}^{21}$  are consistent with our transport measurements, showing a two-fold symmetric angular dependent resistivity that becomes undiscernible above  $T^*$  (Fig. S14).

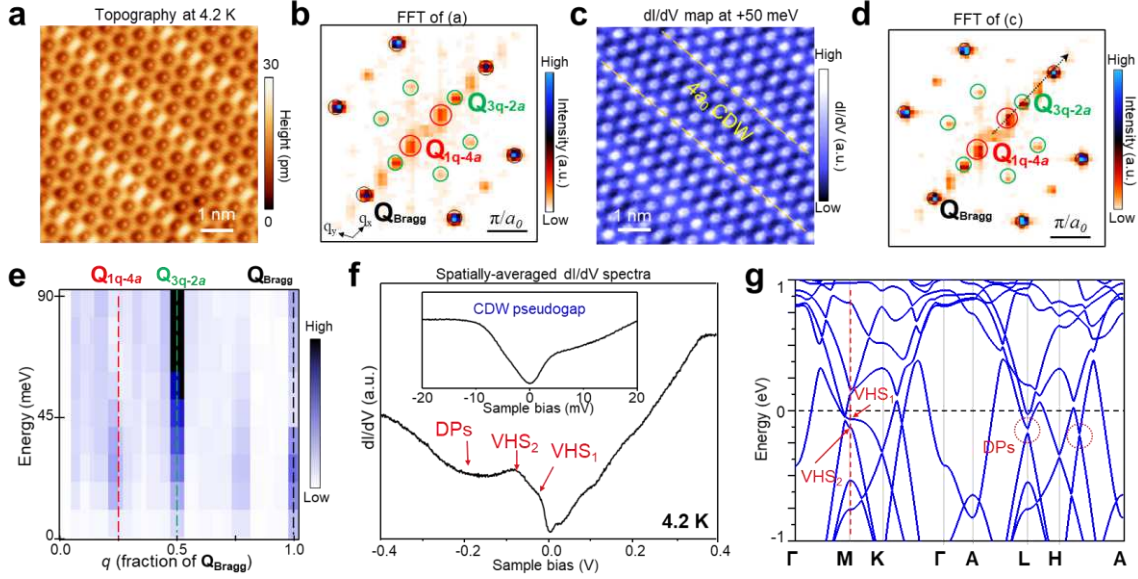


**Fig. 4. Charge ordered normal state and pseudogap in the  $\text{CsV}_3\text{Sb}_5$  above  $T_c$ .** **a,b** Typical atomically-resolved STM topography of Sb surface and corresponding FFT obtained at 4.2 K, showing  $2 \times 2$  and striped CDW order at wave vectors  $\mathbf{Q}_{3q-2a}$  and  $\mathbf{Q}_{1q-4a}$  ( $V_s = -90 \text{ mV}$ ,  $I_t = 2 \text{ nA}$ ). **c, d**  $dI/dV$  mapping of (a) at  $-50 \text{ mV}$  and the corresponding FFT patterns, respectively ( $V_s = -90 \text{ mV}$ ,  $I_t = 2 \text{ nA}$ ,  $V_{mod} = 0.5 \text{ mV}$ ). **e.** FFT line cut along the  $q_x$ -direction as a function of energy, showing that ordering vectors at  $\mathbf{Q}_{3q-2a}$  and  $\mathbf{Q}_{1q-4a}$  are non-dispersive ( $V_s = -90 \text{ mV}$ ,  $I_t = 2 \text{ nA}$ ,  $V_{mod} = 0.5 \text{ mV}$ ). **f,** Spatially-averaged  $dI/dV$  spectra obtained on the Sb surface at 4.2 K. Signatures of the Dirac and VHS points are marked by the red arrows. ( $V_s = -0.4 \text{ V}$ ,  $I_t = 0.5 \text{ nA}$ ,  $V_{mod} = 5 \text{ mV}$ ). Inset: Small scale  $dI/dV$  spectrum in the range of  $(-20 \text{ mV}, 20 \text{ mV})$ , showing the CDW induced pseudogap. ( $V_s = -20 \text{ mV}$ ,  $I_t = 1 \text{ nA}$ ,  $V_{mod} = 0.5 \text{ mV}$ ) **g,** The calculated electronic band structure of  $\text{CsV}_3\text{Sb}_5$  with the Dirac and VHS points marked for comparison to (f).

## Discussion

Unconventional superconductivity with various angular momentum pairing symmetries can arise in model calculations from local and extended electron correlations on the kagome lattice<sup>53-55</sup>. We stress, however, that the physics discovered here goes well beyond that  $\text{CsV}_3\text{Sb}_5$  is another unconventional strong-coupling superconductor. It embodies a set of highly provoking quantum electronic states and excitations that show striking analogies and distinctions, and may hold the common set of keys to resolve some of the

outstanding issues in the cuprates high- $T_c$  superconductors, including smectic electronic liquid crystal states,  $4a_0$  unidirectional charge order, pseudogap phenomenology, novel PDW and its interplay with CDW and nodal superconductivity. The stoichiometric kagome lattice compounds are advantageous for disentangling the long-range ordered and fluctuating components in the electronic states. The layered structure in  $AV_3Sb_5$  with Van de Waals interlayer coupling provides further opportunities to obtain one-unit cell two-dimensional kagome materials by exfoliation for deeper exploration of these and other unexpected challenges in the low-energy many-body physics. Our findings provide groundwork and insights for future studies on how the unconventional SC state, the roton-PDW, and the coexisting charge order originate microscopically from the correlated and  $Z_2$  topological kagome bands, and on the prospects of emergent topological superconductivity in  $AV_3Sb_5$ .

## Methods

**Single crystal growth of CsV<sub>3</sub>Sb<sub>5</sub> sample.** Single crystals of CsV<sub>3</sub>Sb<sub>5</sub> were grown from Cs liquid (purity 99.98%), V powder (purity 99.9%) and Sb shot (purity 99.999%) via a modified self-flux method<sup>15</sup>. The mixture was put into an alumina crucible and sealed in a quartz ampoule under Argon atmosphere. The mixture was heated to 1000 °C and soaked for 24 h, and subsequently cooled at 2 °C/h. Finally, the single crystal was separated from the flux and the residual flux on the surface was carefully removed by a Scotch tape. Except sealing and heat treatment procedures, all of other preparation procedures were carried out in an argon-filled glove box in order to avoid the introduction of any air and water. The obtained crystals have a typical hexagonal morphology with a size of over 2×2×0.3 cm<sup>3</sup> (Fig. S1) and are stable in the air.

**Sample characterization.** XRD pattern was collected using a Rigaku SmartLab SE X-ray diffractometer with Cu K $\alpha$  radiation ( $\lambda = 0.15418$  nm) at room temperature. Scanning electron microscopy (SEM) and energy-dispersive X-ray spectroscopy (EDX) were performed using a HITACHI S5000 with an energy dispersive analysis system Bruker XFlash 6|60. Magnetic susceptibility were determined by a SQUID magnetometer (Quantum Design MPMS XL-1). The SC transition of each sample was monitored down to 2 K under an external magnetic field of 1 Oe. Both in-plane electrical resistivity and Hall resistivity data were collected on a Quantum Design Physical Properties Measurement System (PPMS).

**Scanning tunneling microscopy/spectroscopy and Josephson STS.** The samples used in the experiments are cleaved *room temperature* and immediately transferred to an STM chamber. Experiments were performed in an ultrahigh vacuum ( $1 \times 10^{-10}$  mbar) ultra-low temperature STM system equipped with 9-2-2 T magnetic field. The electronic temperature in the low-temperature STS is calibrated using a standard superconductor, Nb crystal. All the scanning parameters (setpoint voltage and current) of the STM topographic images are listed in the captions of the figures. Unless otherwise noted, the differential conductance ( $dI/dV$ ) spectra were acquired by a standard lock-in amplifier at a modulation frequency of 973.1 Hz. Non-superconducting tungsten tip was fabricated via electrochemical etching and calibrated on a clean Au(111) surface prepared by repeated cycles of sputtering with argon ions and annealing at 500 °C. Superconducting Nb tip was applied in the Josephson STM measurement. The Nb tip was fabricated via mechanical cut of a Nb rod and calibrated on a clean Nb(110) surface prepared by repeated cycles of sputtering with argon ions and annealing at 1200 °C (Fig. S7).

**DFT calculations.** All calculations were performed within the Density Functional Theory as implemented in the Vienna Ab-initio Simulation Package (VASP)<sup>56,57</sup>. The exchange-correlation functional were treated with in the generalized gradient approximation as parametrized by Perdew-Burke-Ernzerhof<sup>58</sup>. The cutoff energy for the plane-wave basis set is 300 eV. The zero damping DFT-D3 van der Waals correction<sup>59</sup> is employed in all the calculations. Spin-orbital coupling (SOC) is considered in the band structure calculations. *k*-meshes of 9×9×6 and 6×6×6 are used for calculating electronic structures of the pristine phase and 2×2 CDW phase, respectively. The phonon dispersions are calculated (without SOC) by using the phonopy code<sup>60</sup> within a 3×3×2 supercell for the pristine structure and 2×2×2 supercells for 2×2 CDW phases.

### **Data availability**

Data measured or analyzed during this study are available from the corresponding author on reasonable request.

### **Acknowledgements**

We thank Zhong-Xian Zhao, Ilija Zeljkovic and Jiaxin Yin for helpful discussions. The work is supported by grants from the National Natural Science Foundation of China (61888102, 52022105, 11974422 and 11974394), the National Key Research and Development Projects of China (2016YFA0202300, 2017YFA0206303, 2018YFA0305800, 2019YFA0308500 and 2019YFA0704900), and the Chinese Academy of Sciences (XDB28000000, 112111KYSB20160061). Z.W. is supported by the US DOE, Basic Energy Sciences Grant No. DE-FG02-99ER45747.

**Author Contributions:** H.-J.G. designed the experiments. H.C., B.H., Y.X., G.Q, Z.H., Y.Y., C.S., G.L. performed STM experiments with guidance of H.-J.G. H.Y. and H.L. prepared samples. X.D, J.Y, H.Y., S.M., H.Z. and S.N. performed the transport experiments. Z.W., S.Z., H.T. and B.Y. carried out theoretical work. All of the authors participated in analyzing experimental data, plotting figures, and writing the manuscript. H.-J. G. and Z.W. supervised the project.

**Competing Interests:** The authors declare that they have no competing interests.

## References

- 1 Balents, L. Spin liquids in frustrated magnets. *Nature* **464**, 199-208 (2010).
- 2 Helton, J. *et al.* Spin dynamics of the spin-1/2 kagome lattice antiferromagnet  $\text{ZnCu}_3(\text{OH})_6\text{Cl}_2$ . *Phys. Rev. Lett.* **98**, 107204 (2007).
- 3 Ko, W.-H., Lee, P. A. & Wen, X.-G. Doped kagome system as exotic superconductor. *Phys. Rev. B* **79**, 214502 (2009).
- 4 Han, T.-H. *et al.* Fractionalized excitations in the spin-liquid state of a kagome-lattice antiferromagnet. *Nature* **492**, 406-410 (2012).
- 5 Fu, M., Imai, T., Han, T.-H. & Lee, Y. S. Evidence for a gapped spin-liquid ground state in a kagome Heisenberg antiferromagnet. *Science* **350**, 655-658 (2015).
- 6 Ye, L. D. *et al.* Massive Dirac fermions in a ferromagnetic kagome metal. *Nature* **555**, 638-642 (2018).
- 7 Yin, J. X. *et al.* Giant and anisotropic many-body spin-orbit tunability in a strongly correlated kagome magnet. *Nature* **562**, 91-95 (2018).
- 8 Liu, Z. *et al.* Orbital-selective Dirac fermions and extremely flat bands in frustrated kagome-lattice metal  $\text{CoSn}$ . *Nat. Commun.* **11**, 4002 (2020).
- 9 Morali, N. *et al.* Fermi-arc diversity on surface terminations of the magnetic Weyl semimetal  $\text{Co}_3\text{Sn}_2\text{S}_2$ . *Science* **365**, 1286-1291 (2019).
- 10 Liu, D. F. *et al.* Magnetic Weyl semimetal phase in a Kagomé crystal. *Science* **365**, 1282-1285 (2019).
- 11 Kuroda, K. *et al.* Evidence for magnetic Weyl fermions in a correlated metal. *Nat. Mater.* **16**, 1090 (2017).
- 12 Yin, J. X. *et al.* Quantum-limit Chern topological magnetism in  $\text{TbMn}_6\text{Sn}_6$ . *Nature* **583**, 533-536 (2020).
- 13 Yin, J.-X. *et al.* Negative flat band magnetism in a spin-orbit-coupled correlated kagome magnet. *Nat. Phys.* **15**, 443-448 (2019).
- 14 Xing, Y. *et al.* Localized spin-orbit polaron in magnetic Weyl semimetal  $\text{Co}_3\text{Sn}_2\text{S}_2$ . *Nat. Commun.* **11**, 5613 (2020).
- 15 Ortiz, B. R. *et al.* New kagome prototype materials: discovery of  $\text{KV}_3\text{Sb}_5$ ,  $\text{RbV}_3\text{Sb}_5$ , and  $\text{CsV}_3\text{Sb}_5$ . *Phys. Rev. Mater.* **3** (2019).
- 16 Ortiz, B. R. *et al.*  $\text{CsV}_3\text{Sb}_5$ : A  $\mathbb{Z}_2$  Topological Kagome Metal with a Superconducting Ground State. *Phys. Rev. Lett.* **125**, 247002 (2020).
- 17 Kenney, E. M., Ortiz, B. R., Wang, C., Wilson, S. D. & Graf, M. J. Absence of local moments in the kagome metal  $\text{KV}_3\text{Sb}_5$  as determined by muon spin spectroscopy. *Arxiv:2012.04737* (2020).
- 18 Ortiz, B. R. & Sarte, P. M. Superconductivity in the  $\mathbb{Z}_2$  kagome metal  $\text{KV}_3\text{Sb}_5$ . *Arxiv:2012.09097* (2020).
- 19 Yin, Q. *et al.* Superconductivity and normal-state properties of kagome metal  $\text{RbV}_3\text{Sb}_5$  single crystals. *Arxiv:2101.10193* (2021).
- 20 Jiang, Y.-X. *et al.* Discovery of topological charge order in kagome superconductor  $\text{KV}_3\text{Sb}_5$ . *Arxiv:2012.15709* (2020).
- 21 Zhao, H. *et al.* Cascade of correlated electron states in a kagome superconductor  $\text{CsV}_3\text{Sb}_5$ . *Arxiv:2103.03118* (2021).

- 22 Liang, Z. *et al.* Three-dimensional charge density wave and robust zero-bias conductance peak inside the superconducting vortex core of a kagome superconductor CsV<sub>3</sub>Sb<sub>5</sub>. *Arxiv:2103.04760* (2021).
- 23 Yang, S.-Y. *et al.* Giant, unconventional anomalous Hall effect in the metallic frustrated magnet candidate, KV<sub>3</sub>Sb<sub>5</sub>. *Sci. Adv.* **6**, eabb6003 (2020).
- 24 Yu, F. H. *et al.* Concurrence of anomalous Hall effect and charge density wave in a superconducting topological kagome metal. *Arxiv:2102.10987* (2021).
- 25 Wang, Y. *et al.* Proximity-induced spin-triplet superconductivity and edge supercurrent in the topological Kagome metal, K<sub>1-x</sub>V<sub>3</sub>Sb<sub>5</sub>. *Arxiv:2012.05898* (2020).
- 26 Zhao, C. C. *et al.* Nodal superconductivity and superconducting dome in the topological Kagome metal CsV<sub>3</sub>Sb<sub>5</sub>. *Arxiv:2102.08356* (2021).
- 27 Hamidian, M. H. *et al.* Detection of a Cooper-pair density wave in Bi<sub>2</sub>Sr<sub>2</sub>CaCu<sub>2</sub>O<sub>8+x</sub>. *Nature* **532**, 343-347 (2016).
- 28 Ruan, W. *et al.* Visualization of the periodic modulation of Cooper pairing in a cuprate superconductor. *Nat. Phys.* **14**, 1178-1182 (2018).
- 29 Du, Z. *et al.* Imaging the energy gap modulations of the cuprate pair-density-wave state. *Nature* **580**, 65-70 (2020).
- 30 Li, X. *et al.* Evolution of Charge and Pair Density Modulations in Overdoped Bi<sub>2</sub>Sr<sub>2</sub>CuO<sub>6+δ</sub>. *Phys. Rev. X* **11**, 011007 (2021).
- 31 Agterberg, D. F. *et al.* The Physics of Pair-Density Waves: Cuprate Superconductors and Beyond. *Annu. Rev. Condens. Matter Phys.* **11**, 231-270 (2020).
- 32 Chen, H. *et al.* Evidence for Ultralow-Energy Vibrations in Large Organic Molecules. *Nano Lett.* **17**, 4929-4933 (2017).
- 33 Hirjibehedin, C. F. *et al.* Large magnetic anisotropy of a single atomic spin embedded in a surface molecular network. *Science* **317**, 1199-1203 (2007).
- 34 Cho, D., Bastiaans, K. M., Chatzopoulos, D., Gu, G. D. & Allan, M. P. A strongly inhomogeneous superfluid in an iron-based superconductor. *Nature* **571**, 541-545 (2019).
- 35 Pan, S. H., Hudson, E. W. & Davis, J. C. Vacuum tunneling of superconducting quasiparticles from atomically sharp scanning tunneling microscope tips. *Appl. Phys. Lett.* **73**, 2992-2994 (1998).
- 36 Rodrigo, J. G., Suderow, H., Vieira, S., Bascones, E. & Guinea, F. Superconducting nanostructures fabricated with the scanning tunnelling microscope. *J. Phys.: Condens. Matter* **16**, R1151-R1182 (2004).
- 37 Naaman, O., Teizer, W. & Dynes, R. C. Fluctuation Dominated Josephson Tunneling with a Scanning Tunneling Microscope. *Phys. Rev. Lett.* **87**, 097004 (2001).
- 38 Kimura, H., Barber, R. P., Ono, S., Ando, Y. & Dynes, R. C. Josephson scanning tunneling microscopy: A local and direct probe of the superconducting order parameter. *Phys. Rev. B* **80**, 144506 (2009).
- 39 Šmakov, J., Martin, I. & Balatsky, A. V. Josephson scanning tunneling microscopy. *Phys. Rev. B* **64**, 212506 (2001).
- 40 Proslir, T. *et al.* Probing the superconducting condensate on a nanometer scale. *EPL* **73**, 962-968 (2006).
- 41 Fischer, Ø., Kugler, M., Maggio-Aprile, I., Berthod, C. & Renner, C. Scanning tunneling spectroscopy of high-temperature superconductors. *Rev. Mod. Phys.* **79**, 353-419 (2007).
- 42 Jiao, L. *et al.* Chiral superconductivity in heavy-fermion metal UTe<sub>2</sub>. *Nature* **579**, 523-527 (2020).

- 43 Kivelson, S. A., Fradkin, E. & Emery, V. J. Electronic liquid-crystal phases of a doped Mott insulator. *Nature* **393**, 550-553 (1998).
- 44 Emery, V. J., Fradkin, E., Kivelson, S. A. & Lubensky, T. C. Quantum theory of the smectic metal state in stripe phases. *Phys. Rev. Lett.* **85**, 2160 (2000).
- 45 Agterberg, D. & Tsunetsugu, H. Dislocations and vortices in pair-density-wave superconductors. *Nat. Phys.* **4**, 639-642 (2008).
- 46 Berg, E., Fradkin, E. & Kivelson, S. A. Charge-4 e superconductivity from pair-density-wave order in certain high-temperature superconductors. *Nat. Phys.* **5**, 830-833 (2009).
- 47 Lee, P. A. Amperean pairing and the pseudogap phase of cuprate superconductors. *Phys. Rev. X* **4**, 031017 (2014).
- 48 Landau, L. On the Theory of Superfluidity. *Phys. Rev.* **75**, 884-885 (1949).
- 49 Feynman, R. P. in *Progress in Low Temperature Physics* Vol. 1 (ed C. J. Gorter) 17-53 (Elsevier, 1955).
- 50 Feynman, R. P. & Cohen, M. Energy Spectrum of the Excitations in Liquid Helium. *Phys. Rev.* **102**, 1189-1204 (1956).
- 51 Nozières, P. Is the Roton in Superfluid 4He the Ghost of a Bragg Spot? *J. Low Temp. Phys.* **137**, 45-67 (2004).
- 52 Tan, H., Liu, Y., Wang, Z. & Yan, B. Charge density waves and electronic properties of superconducting kagome metals. *Arxiv:2103.06325* (2021).
- 53 Yu, S. L. & Li, J. X. Chiral superconducting phase and chiral spin-density-wave phase in a Hubbard model on the kagome lattice. *Phys. Rev. B* **85**, 144402 (2012).
- 54 Kiesel, M. L., Platt, C. & Thomale, R. Unconventional Fermi Surface Instabilities in the Kagome Hubbard Model. *Phys. Rev. Lett.* **110**, 126405 (2013).
- 55 Wang, W. S., Li, Z. Z., Xiang, Y. Y. & Wang, Q. H. Competing electronic orders on kagome lattices at van Hove filling. *Phys. Rev. B* **87**, 115135 (2013).
- 56 Kresse, G. & Furthmuller, J. Efficiency of ab-initio total energy calculations for metals and semiconductors using a plane-wave basis set. *Comp. Mater. Sci.* **6**, 15-50 (1996).
- 57 Kresse, G. & Furthmuller, J. Efficient iterative schemes for ab initio total-energy calculations using a plane-wave basis set. *Phys. Rev. B* **54**, 11169-11186 (1996).
- 58 Perdew, J. P., Burke, K. & Ernzerhof, M. Generalized gradient approximation made simple. *Phys. Rev. Lett.* **77**, 3865-3868 (1996).
- 59 Grimme, S., Antony, J., Ehrlich, S. & Krieg, H. A consistent and accurate ab initio parametrization of density functional dispersion correction (DFT-D) for the 94 elements H-Pu. *J. Chem. Phys.* **132** (2010).
- 60 Togo, A. & Tanaka, I. First principles phonon calculations in materials science. *Scr. Mater.* **108**, 1-5 (2015).

# Figures

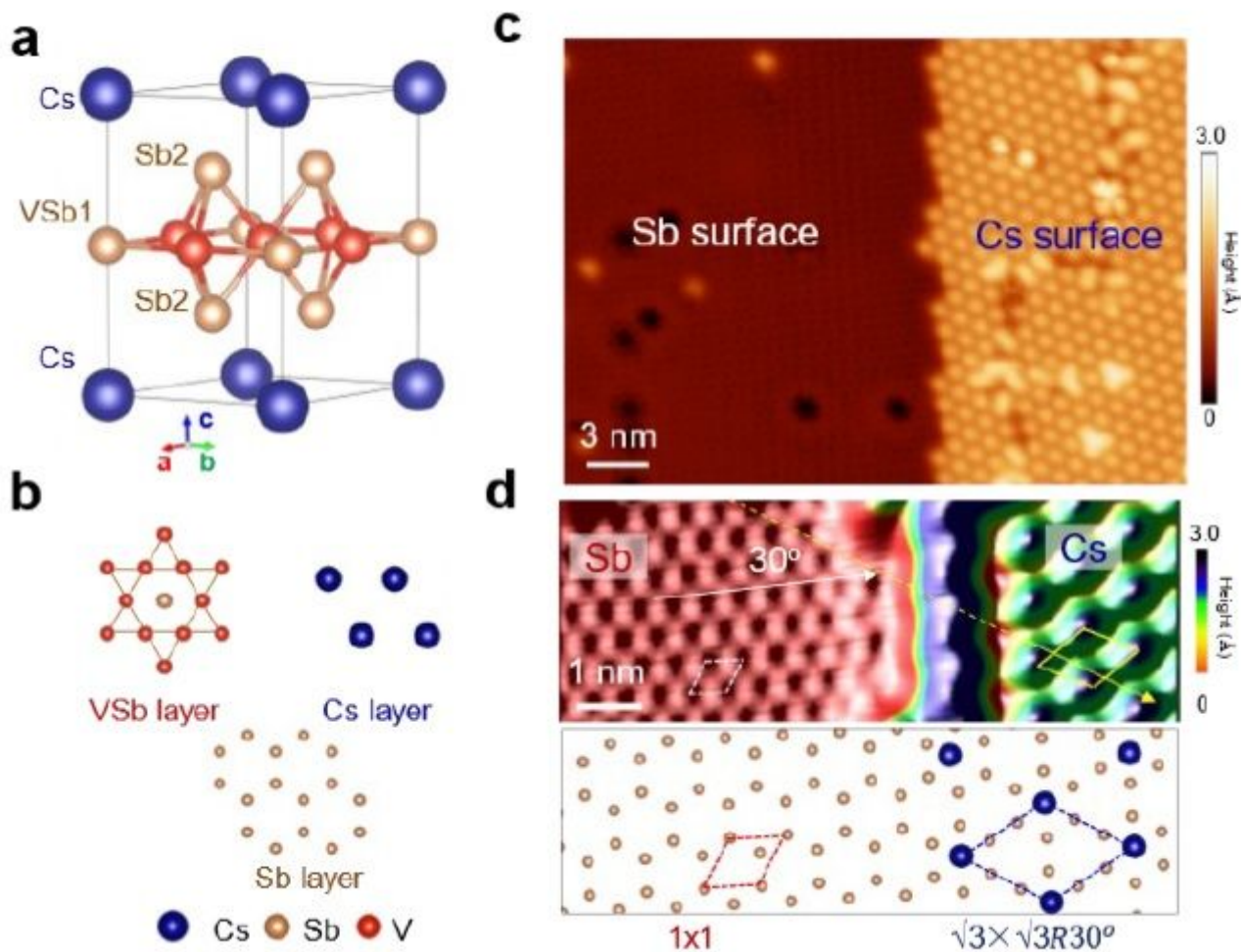


**Figure 1**

Atomic structures and the surface identification of the CsV<sub>3</sub>Sb<sub>5</sub>. a, 3D view of crystal structure, showing stacking of Cs-Sb<sub>2</sub>-VSb<sub>1</sub>-Sb<sub>2</sub>-Cs layers with hexagonal symmetry. b, Atomic structures of VSb, Cs and Sb layers. c, Typical large-scale STM image, showing the Cs surface and Sb surface, respectively (scanning setting: bias: V<sub>s</sub>=-1.0 V, setpoint I<sub>t</sub>=100 pA). d, Typical atomically-resolved STM image, showing the atomic structures of the Cs surface and the Sb surface, respectively (V<sub>s</sub>=-0.5 V, I<sub>t</sub>=500 pA). Bottom panel: schematic of the atomic structures of the Sb and Cs surfaces, showing 1×1 and  $\sqrt{3} \times \sqrt{3} R 30^\circ$  reconstructed structures, respectively.

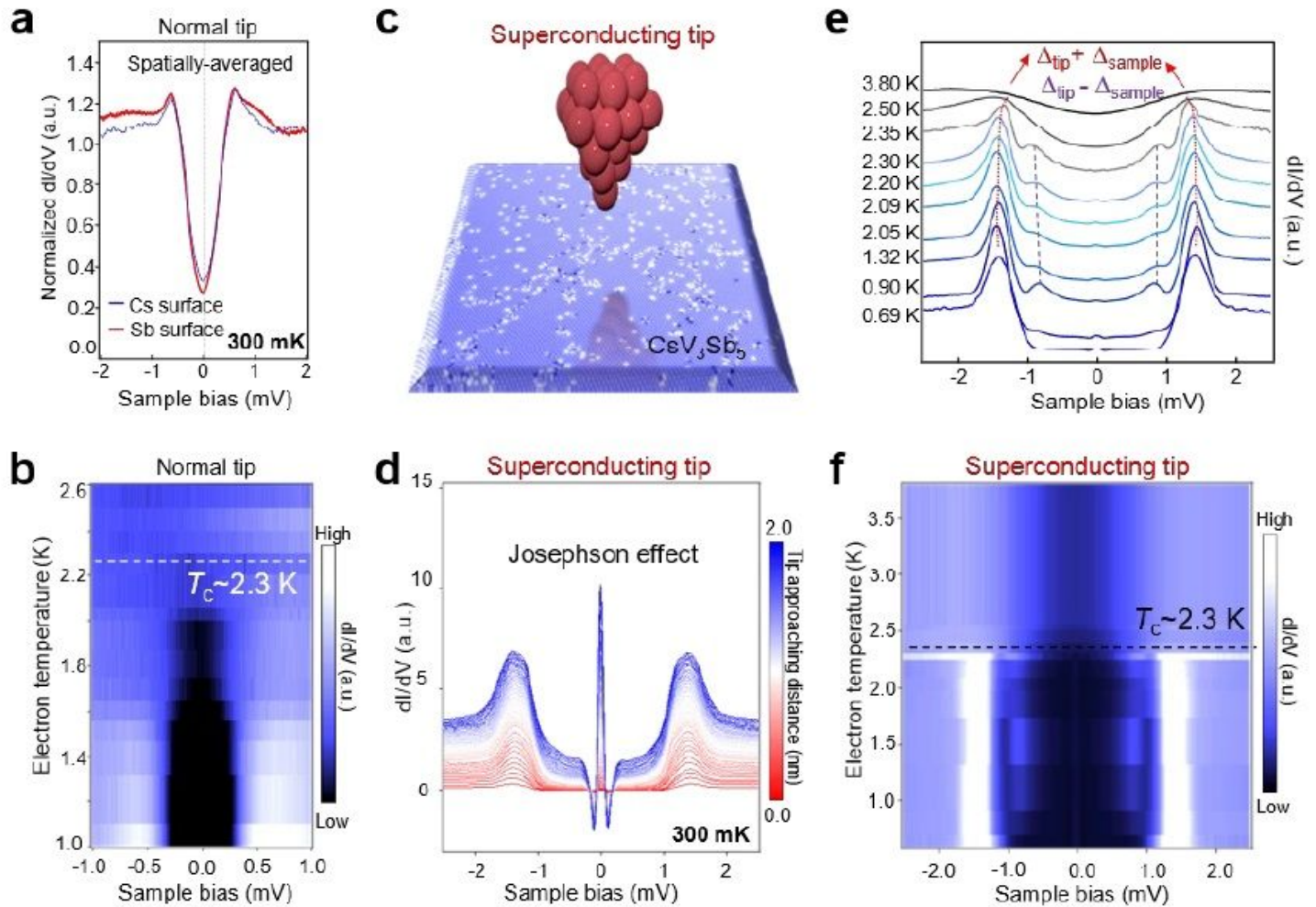


**Figure 2**

V-shaped pairing gap and the Josephson effect observed using a superconducting STM tip on the Cs and Sb surfaces. a, Spatially-averaged  $dI/dV$  spectra obtained on the Cs and Sb surfaces over a  $30 \text{ nm} \times 30 \text{ nm}$  region with small defect density at the Telectron = 300 mK, showing a particle-hole symmetric V-shaped gap near EF and non-zero LDOS at zero-bias ( $V_s = -2 \text{ mV}$ ,  $I_t = 1 \text{ nA}$ ,  $V_{\text{mod}} = 50 \text{ } \mu\text{V}$ ). b, Color map of temperature dependent  $dI/dV$  spectra obtained on the Cs surface, showing that the V-shaped gap reduces with increasing electron temperature and vanishes around  $\sim 2.3 \text{ K}$  (dotted white line) ( $V_s = -2 \text{ mV}$ ,  $I_t = 1 \text{ nA}$ ,  $V_{\text{mod}} = 50 \text{ } \mu\text{V}$ ). c, Schematics showing the Josephson STM on  $\text{CsV}_3\text{Sb}_5$  surface using a superconducting (Nb) tip. d, A series of  $dI/dV$  spectra with approaching tip toward sample surface. A sharp zero-bias peak with two negative differential conductance dips are observed, providing strong evidence that the  $\text{CsV}_3\text{Sb}_5$  is in the SC phase ( $V_s = -2.5 \text{ mV}$ ,  $V_{\text{mod}} = 50 \text{ } \mu\text{V}$ ). e, Temperature dependent  $dI/dV$  spectra on the Cs surface using a Nb tip, showing two energy gaps at  $\Delta_{\text{tip}} + \Delta_{\text{sample}}$  and  $\Delta_{\text{tip}} - \Delta_{\text{sample}}$ , respectively ( $V_s = -2.5 \text{ mV}$ ,  $I_t = 20 \text{ nA}$ ,  $V_{\text{mod}} = 50 \text{ } \mu\text{V}$ ). f, Color map of the  $dI/dV$  spectra in (e), showing the transition temperature of the  $\text{CsV}_3\text{Sb}_5$  sample around  $\sim 2.3 \text{ K}$  ( $V_s = -2.5 \text{ mV}$ ,  $I_t = 20 \text{ nA}$ ,  $V_{\text{mod}} = 50 \text{ } \mu\text{V}$ ).

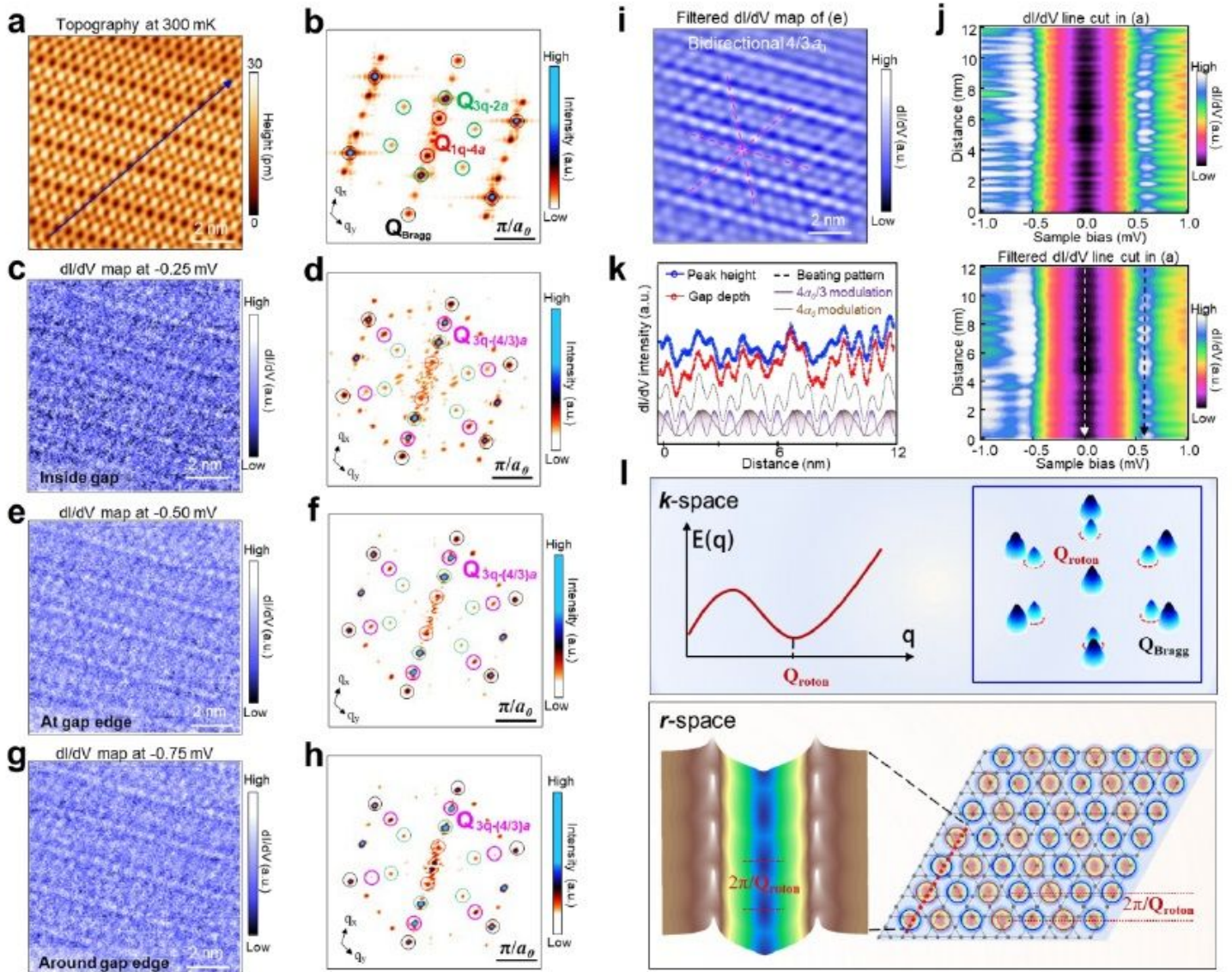


**Figure 3**

Spatial distribution of quantum electronic states on Sb surface at  $T=300$  mK. a, Typical atomically-resolved STM topography of Sb surface ( $V_s=-90$  mV,  $I_t=2$  nA). b, FFT of (a), showing clearly wave vectors  $Q_{3q-2a}$  associated with  $2 \times 2$  CDW and  $Q_{1q-4a}$  associated with  $4a_0$  unidirectional charge order. c, e, g  $dI/dV$  maps of (a) at  $-0.25$  meV,  $-0.5$  meV and  $-0.75$  meV, respectively ( $V_s=-90$  mV,  $I_t=2$  nA,  $V_{mod}=0.2$  mV). d, f, h FFT patterns corresponding to (c), (e) and (g), respectively. Besides the  $Q_{3q-2a}$  and  $Q_{1q-4a}$  charge ordered states present in the topography (a, b), a new  $4a_0/3$  bidirectional modulation emerges at  $Q_{3q-4a/3}$ . i, The  $dI/dV$  map near the pairing gap in (e) after filtering out atomic Bragg peaks at  $Q_{Bragg}$  and incoherent background, showing  $4a_0/3$  checkerboard modulations associated with the bidirectional PDW. j. Image plot of the  $dI/dV$  curves along a line cut in the lattice direction shown in (a), before (upper panel) and after (lower panel) filtering ( $V_s=-1$  mV,  $I_t=4$  nA,  $V_{mod}=20$   $\mu$ V). k, Spatial modulations of the coherence peak height (blue curve) along the black arrow in (j) and the SC gap-depth (red curve) obtained by subtracting the zero-bias conductance along the white arrow in (j) from the peak

height, showing strong positive correlation between the two curves. The simulated curve based on Q1q-4a (brown curve) and Q3q-4a/3 (purple curve) modulations shows a beating pattern consistent with the coherence peak height and gap-depth modulations. I, Schematic illustrations of the roton-PDW. Top panel: the roton dispersion and minimum at Qroton in the reciprocal lattice. Bottom panel: the bidirectional roton-PDW at  $Q_{pdw} = Q_{roton}/2$  forming a commensurate vortex-antivortex (blue and red circles) lattice that spatially modulates the tunneling conductance spectra along a line cut.

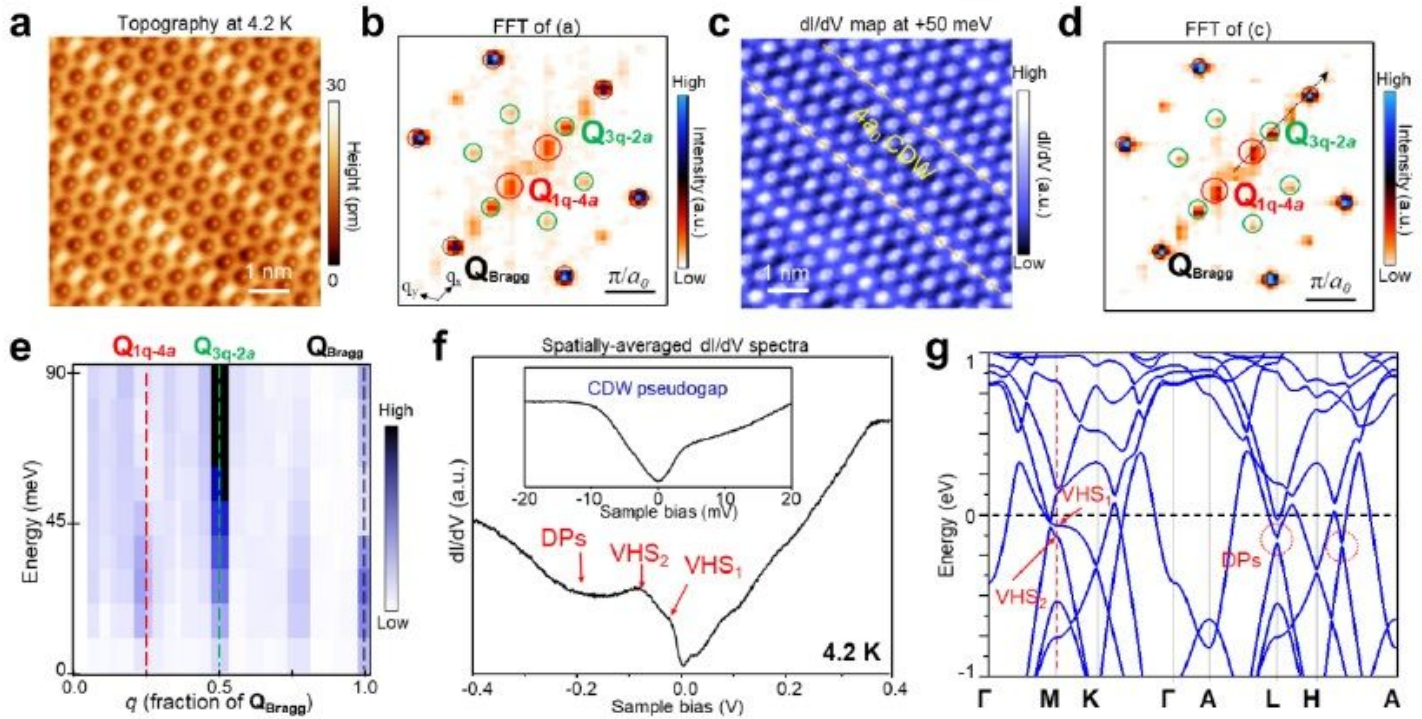


**Figure 4**

Charge ordered normal state and pseudogap in the CsV3Sb5 above  $T_c$ . a,b Typical atomically-resolved STM topography of Sb surface and corresponding FFT obtained at 4.2 K, showing  $2 \times 2$  and striped CDW order at wave vectors  $Q_{3q-2a}$  and  $Q_{1q-4a}$  ( $V_s = -90$  mV,  $I_t = 2$  nA). c, d  $dI/dV$  mapping of (a) at -50 mV and the corresponding FFT patterns, respectively ( $V_s = -90$  mV,  $I_t = 2$  nA,  $V_{mod} = 0.5$  mV). e. FFT line cut along the  $q_x$ -direction as a function of energy, showing that ordering vectors at  $Q_{3q-2a}$  and  $Q_{1q-4a}$  are non-dispersive ( $V_s = -90$  mV,  $I_t = 2$  nA,  $V_{mod} = 0.5$  mV). f, Spatially-averaged  $dI/dV$  spectra obtained on the Sb surface at 4.2 K. Signatures of the Dirac and VHS points are marked by the red arrows. ( $V_s = -0.4$  V,  $I_t = 0.5$  nA,  $V_{mod} = 5$  mV). Inset: Small scale  $dI/dV$  spectrum in the range of (-20 mV, 20 mV), showing the CDW induced pseudogap. ( $V_s = -20$  mV,  $I_t = 1$  nA,  $V_{mod} = 0.5$  mV) g, The calculated electronic band structure of CsV3Sb5 with the Dirac and VHS points marked for comparison to (f).

## Supplementary Files

This is a list of supplementary files associated with this preprint. [Click to download.](#)

- [CsV3Sb5SI20210323f.pdf](#)